

AperTO - Archivio Istituzionale Open Access dell'Università di Torino

Carboniferous high-pressure metamorphism of Ordovician protoliths in the Argentera Massif (Italy), Southern European Variscan belt.

This is the author's manuscript

Original Citation:

Availability:

This version is available <http://hdl.handle.net/2318/76326> since

Published version:

DOI:10.1016/j.lithos.2009.12.013

Terms of use:

Open Access

Anyone can freely access the full text of works made available as "Open Access". Works made available under a Creative Commons license can be used according to the terms and conditions of said license. Use of all other works requires consent of the right holder (author or publisher) if not exempted from copyright protection by the applicable law.

(Article begins on next page)



UNIVERSITÀ DEGLI STUDI DI TORINO

This Accepted Author Manuscript (AAM) is copyrighted and published by Elsevier. It is posted here by agreement between Elsevier and the University of Turin. Changes resulting from the publishing process - such as editing, corrections, structural formatting, and other quality control mechanisms - may not be reflected in this version of the text. The definitive version of the text was subsequently published in *Lithos*, **116**, 65-76. doi:10.1016/j.lithos.2009.12.013.

You may download, copy and otherwise use the AAM for non-commercial purposes provided that your license is limited by the following restrictions:

- (1) You may use this AAM for non-commercial purposes only under the terms of the CC-BY-NC-ND license.
- (2) The integrity of the work and identification of the author, copyright owner, and publisher must be preserved in any copy.
- (3) You must attribute this AAM in the following format: Creative Commons BY-NC-ND license (<http://creativecommons.org/licenses/by-nc-nd/4.0/deed.en>), doi:10.1016/j.lithos.2009.12.013

1

2 **Carboniferous high-pressure metamorphism of Ordovician protoliths**
3 **in the Argentera Massif (Italy), Southern European Variscan belt**

4

5 **Daniela Rubatto** 

6 Research School of Earth Sciences, The Australian National University, Canberra
7 0200, Australia

8

9 **Simona Ferrando, Roberto Compagnoni**

10 Dipartimento di Scienze Mineralogiche e Petrologiche, Universita' degli Studi di
11 Torino, Via Valperga Caluso 35, Torino 10125, Italy

12

13 **Bruno Lombardo**

14 C.N.R., Istituto di Geoscienze e Georisorse, Via Valperga Caluso 35, Torino 10125,
15 Italy

16

17  Daniela.rubatto@anu.edu.au

18 Tel. ++61 (0)2 6125 5157

19 Fax ++61 (0)2 6125 0941

20

21

22

23

24 **ABSTRACT**

25 The age of high-pressure metamorphism is crucial to identify a suitable tectonic
26 model for the vast Variscan orogeny. Banded *HP* granulites from the Gesso-Stura
27 Terrain in the Argentera Massif, Italy, have been recently described (Ferrando et al.,
28 2008) as relict of high-pressure metamorphism in the western part of the Variscan
29 orogen. Bulk rock chemistry of representative lithologies reveals intermediate silica
30 contents and calc-alkaline affinity of the various cumulate layers. Enrichment in
31 incompatible elements denotes a significant crustal component in line with intrusion
32 during Ordovician rifting. Magmatic zircon cores from a Pl-rich layer yield scattered
33 ages indicating a minimum protolith age of 486 ± 7 Ma. Carboniferous zircons
34 (340.7 ± 4.2 and 336.3 ± 4.1 Ma) are found in a Pl-rich and a Pl-poor layer,
35 respectively. Their zoning, chemical composition (low Th/U, flat HREE pattern and Ti-
36 in-zircon temperature) and deformation indicate that they formed during the high-
37 pressure event before decompression and mylonitisation. The proposed age for high-
38 pressure metamorphism in the Argentera Massif proves that subduction preceded
39 anatexis by less than 20 Ma. The new data allow a first-order comparison with the
40 Bohemian Massif, which is located at the eastern termination of the Variscan orogen.
41 Similarities in evolution at either end of the orogen support a Himalayan-type
42 tectonic model for the entire European Variscides.

43 **Keywords HP granulites, U-Pb geochronology, zircon, Variscan belt.**

44

45

46 **1. Introduction**

47 The Variscan orogeny (~380-300 Ma) is the geological event most largely
48 represented in the basement of the European continent. It was assembled between
49 Ordovician and Carboniferous from the larger collision of Gondwana with the
50 northern plate of Laurentia-Baltica, which involved the microplates of Avalonia and
51 Armorica (Matte, 2001). Variscan units extend from southern Spain (the Ibero-
52 Armorican termination) to Poland (the Bohemian Massif). Large remnants of Variscan
53 basement are preserved in the southern Variscides, within the Alpine chain, where
54 they are located in external positions. In the Western and Central Alps, such
55 remnants are identified as External Crystalline Massifs, which record the general
56 evolution common to all Pangean Europe (von Raumer et al., 2009).

57 A series of tectonic models have been proposed for the assembly of this vast
58 orogen. Early models favour Himalayan-style collision with subduction of a small
59 ocean rapidly followed by intense continent-continent collision leading to Barrovian
60 metamorphism and extensive crustal anatexis in the Late Carboniferous (summary in
61 O'Brien, 2000). More recently, Andean-style tectonics has been proposed, at least for
62 the eastern termination of Variscan Europe (Bohemian Massif). The Andean model
63 prefers a long lasting subduction process with development of blueschist terranes,
64 extensive arc magmatism in the upper plate and formation of back-arc basins
65 (Schulmann et al., 2009).

66 One crucial piece of information that is necessary in order to better define a
67 suitable geodynamic model for the Variscan orogen is the absolute and relative ages
68 of subduction (as seen in relicts of eclogites) versus the onset of regional anatexis.
69 Whereas the latter event is reasonably well constrained across the western European
70 Variscan basement at around 320-310 Ma (e.g. Demoux et al., 2008; Rubatto et al.,
71 2001), the scarcity of eclogite facies rocks and their poor preservation have

72 hampered robust dating of Variscan high-pressure (*HP*) assemblages. Some
73 constraints exist for the eastern part of the orogen (Bohemian Massif, Kröner et al.,
74 2000; Schulmann et al., 2005), but ages of *HP* assemblages are lacking in the
75 western part. This contribution presents the first geochronological constraints
76 (SHRIMP U-Pb dating of zircon) on *HP* assemblages recently described in the
77 Argentera Massif. This is a crucial record for the External Crystalline Massifs and for
78 most of the western portion of the European Variscan orogen.

79

80 **2. Geological background and previous geochronology**

81 The Argentera Massif is located in NW Italy, on the border with France. It is the
82 southernmost of the External Crystalline Massifs, which are a series of large crustal
83 bodies aligned on the external part of the western and central Alpine chain (Fig. 1a).
84 They are generally composed of a complex Variscan basement intruded by Permian
85 granitoids. Alpine overprint in these Massifs is weak and commonly limited to shear
86 zones. The exhumation of the External Crystalline Massifs from below the Alpine
87 sediments initiated in the Miocene (e.g. Bigot-Cormier et al., 2006), at the end of the
88 Alpine orogeny.

89 The Argentera Massif is largely composed of Variscan migmatites with abundant
90 relicts of pre-anatectic rock types. At the centre of the Massif, a post-Variscan
91 granite (the Central Granite, Fig. 1b) cuts across the foliation. The Massif is
92 subdivided into two major complexes on the basis of different lithological
93 associations: the Gesso-Stura Terrain in the NE, and the Tinée Terrain in the SW. A
94 large shear zone, the Ferriere-Mollières Line, separates the two Terrains. The studied
95 Frisson Lakes area is located at the eastern tip of the Gesso-Stura Terrain, which is

96 mainly composed of migmatitic ortho- and para-gneisses, with various intrusive
97 bodies from mafic (Bousset-Valmasque Complex) to granitic in composition.

98 A Late- to Mid-Carboniferous age ($\leq 323 \pm 12$ Ma) of migmatisation in the
99 Argentera Massif has been proposed on the basis of a zircon lower intercept age
100 obtained for the Meris eclogite (Rubatto et al., 2001), the only relict of fresh eclogite
101 so far dated. Migmatisation in the Gesso-Stura Terrain must have occurred after the
102 intrusion of monzonites (332 ± 3 Ma, Rubatto et al., 2001), which show signs of
103 partial melting, and before the intrusion of the Central Granite (~ 285 - 293 Ma,
104 Ferrara and Malaroda, 1969). For the Tinée Terrain, an earlier age (~ 350 Ma) of
105 metamorphism has been proposed on the basis of scattering Ar-Ar ages of muscovite
106 from gneisses (Monié and Maluski, 1983). Alpine low-grade overprint along shear
107 zones occurred in or before the Early Miocene (Corsini et al., 2004).

108 Additional constraints on Variscan migmatisation come from the nearby massif of
109 Tanneron (Fig. 1a), SE France, where migmatitic rocks contain monazites dated
110 between ~ 317 and 309 Ma (Demoux et al., 2008). In contrast, in Variscan Corsica, a
111 few zircon rims in a migmatitic paragneiss yielded an age of 338 ± 4 Ma (Giacomini et
112 al., 2008), interpreted as dating "incipient migmatisation".

113 Geochronology of pre-anatectic events in the Argentera Massif is scarce and
114 mainly limited to magmatic activity. U-Pb zircon dating has returned the age of Late
115 Ordovician bimodal magmatism (~ 440 and 460 Ma) and of Carboniferous monzonites
116 (Rubatto et al., 2001). Previous attempts to date metamorphic rocks either returned
117 contrasting results (Paquette et al., 1989) or failed to date metamorphism (Rubatto
118 et al., 2001).

119

120 **3. Analytical methods**

121 Whole-rock major- and trace-element compositions were analysed at the Chemex
122 Laboratories (Canada) using ICP-AES (major elements) and ICP-MS (trace elements).
123 The precision for the analyses is better than 1% for major elements and better than
124 5% for trace elements. Zircons were prepared as mineral separates mounted in
125 epoxy and polished down to expose the grain centres. Cathodoluminescence (CL)
126 imaging was carried out at the Electron Microscope Unit, The Australian National
127 University with a HITACHI S2250-N scanning electron microscope working at 15 kV,
128 ~60 μ A and ~20 mm working distance.

129 U-Pb analyses were performed using a sensitive, high-resolution ion microprobe
130 (SHRIMP II) at the Research School of Earth Sciences. Instrumental conditions and
131 data acquisition were generally as described by Williams (1998). The data were
132 collected in sets of six scans throughout the masses. The measured $^{206}\text{Pb}/^{238}\text{U}$ ratio
133 was corrected using reference zircon (417 Ma, Black et al., 2003). Due to the
134 generally low Th/U in the analysed zircons, data were corrected for common Pb on
135 the basis of the measured $^{208}\text{Pb}/^{206}\text{Pb}$ ratio and assuming concordance, as described
136 in Williams (1998). Age calculation was done using the software Isoplot/Ex (Ludwig,
137 2003) and assuming the common Pb composition predicted by Stacey and Kramers
138 (1975). U-Pb data were collected over a single analytical session with a calibration
139 error of 1.6 % (2 sigma). Finally, whenever the error of an average age was less
140 than the calibration error, an error of 1 sigma % was added in quadratic. Average
141 ages are quoted at 95% confidence level (c.l.).

142 Trace element analyses of zircon were performed on the grain mount with a Laser
143 Ablation – ICP-MS at the Research School of Earth Sciences, using a pulsed 193 nm
144 ArF Excimer laser with 100 mJ energy at a repetition rate of 5 Hz (Eggins et al.,
145 1998) coupled to an Agilent 7500 quadrupole ICP-MS. A spot size of 24 or 54 μ m
146 was used according to the dimension of the growth zone of interest. External

147 calibration was performed relative to NIST 612 glass and internal standardisation
148 was based on stoichiometry silica. Accuracy of the analyses was evaluated with a
149 BCR-2G secondary glass standard and is always better than 15%. During the time-
150 resolved analysis, contamination resulting from inclusions, fractures and zones of
151 different composition was monitored for several elements and only the relevant part
152 of the signal was integrated.

153

154 **4. Sample description and chemistry**

155 The two samples investigated are part of a mafic sequence, with mylonitic
156 structure, which consists of alternating layers (up to about 10 cm thick) of Pl-poor and
157 Pl-rich *HP* granulite, and of minor mafic boudins of Pl-poor *HP* granulite (Fig. 2 and
158 3a). The sequence is exposed at Frisson Lakes along the ridge between Val Grande
159 di Vernante and Val Gesso, N of Passo della Mena; in the small hill W of the lower
160 Frisson Lake (2055 m a.s.l.); along the polished outcrops S of the lower Frisson
161 Lake; and in the small hill E of the lower Frisson Lake (Fig. 2). In the field, the mafic
162 sequence constitutes an E-W band, about 200 m thick and 500 m long, surrounded
163 by Variscan migmatitic granitoid gneiss ("biotite anatexite" of Malaroda et al., 1970),
164 *i.e.* the dominant rock type in the area and across the entire Gesso-Stura Terrane.
165 The mafic sequence is elongated in a direction roughly parallel to the general trend
166 of the regional foliation in the Frisson area. However, at the outcrop scale, the
167 mylonitic foliation of the *HP* granulite is cut by the "igneous" fabric of the migmatitic
168 granitoid gneiss. Notably, no sign of melting is observed within the mafic sequence.

169

170 The two samples dated have similar assemblages, but different proportions of
171 major minerals. The Pl-rich *HP* granulite (sample A1553, Fig 3a) has a banded
172 structure and contains plagioclase (35 vol.%), garnet (30 vol.%), quartz (20 vol.%),

173 and minor clinopyroxene, amphibole and biotite (15 vol.%). The mylonitic foliation
174 wraps around large garnet porphyroblasts (0.5-1 cm across) and smaller garnet
175 grains are found in the foliation (Fig. 3b). The Pl-poor *HP* granulite (sample A1554,
176 Fig 3c) occurs as a 10-15 cm thick mafic boudin (Fig. 3a). It mainly consists of
177 garnet (55 vol.%), clinopyroxene (20 vol.%) and amphibole (15 vol.%), whereas
178 plagioclase, biotite and quartz are rare (10 vol.%). The samples were part of the
179 petrographical and petrological study of Ferrando et al. (2008) and we report here
180 only a brief summary of their conclusions.

181 Both rock types contain several generations of minerals which, coupled with
182 thermobarometric data, allow four metamorphic stages to be defined (Fig. 4). The
183 granulite-facies *HP-HT* peak (stage A: $735 \pm 15^\circ\text{C}$, ~ 1.38 GPa) is characterised by the
184 growth of the core of porphyroclastic garnet, and omphacite in stable association
185 with plagioclase, rutile \pm amphibole \pm quartz. The first decompression (stage B
186 $\sim 710^\circ\text{C}$ and 1.10 GPa) corresponds to the growth of the rim of porphyroclastic
187 garnet and omphacite in equilibrium with a second generation of plagioclase, rutile \pm
188 amphibole \pm quartz. Mylonitisation (stage C) was characterised by the growth of
189 neoblastic garnet, diopside, plagioclase, titanite \pm amphibole \pm quartz, and occurred
190 at amphibolite-facies conditions, i.e pressures of 0.85 GPa and still relatively *HT*
191 ($665 \pm 15^\circ\text{C}$). Finally, during stage D ($500 < T < 625^\circ\text{C}$; $P < 0.59$ GPa) plagioclase
192 and amphibole symplectites replaced the rims of garnet and clinopyroxene. No
193 evidence was found for the involvement of the mafic sequence in the anatexis
194 responsible for the Argentera migmatites. Lack of migmatisation of the mafic
195 sequence is attributed to its more refractive composition when compared to the
196 surrounding migmatites (Ferrando et al. 2008).

197 This *P-T* evolution was further supported by pseudosections, which, for the
198 chosen composition, predict mineral assemblages that are consistent with those

199 observed (Ferrando et al., 2008). This evolution and the peak metamorphic
200 conditions are similar to those recorded by relict eclogites within the Argentera
201 Massif (Val Meris eclogite, Colombo, 1996; Rubatto et al., 2001). This and other
202 arguments prompted Ferrando et al. (2008) to conclude that the Frisson Lakes *HP*
203 granulites and the Meris eclogites underwent the same metamorphism and that the
204 two rock types preserve different peak assemblages because of their different bulk
205 composition.

206

207 A mafic boudin (the Pl-poor *HP* granulite of sample A1554) and three layers of the
208 banded *HP* granulite sequence were analysed for bulk rock chemical composition
209 (Table 1). Major element chemistry indicates a common calc-alkaline composition for
210 all four samples. SiO₂ varies between 46 and 56 wt% according to the different
211 proportion of plagioclase+quartz to pyroxene+garnet in the chosen level. The mafic
212 boudin is enriched in Ca, Fe and Mg and depleted in Si and Na with respect to the
213 mafic and intermediate layers (similar to the Pl-rich *HP* granulite of sample A1553)
214 within the banded *HP* granulite sequence. As for trace elements, the four samples
215 have similar trends, with the mafic boudin (A1554) being lower in most elements.
216 Normalized patterns (Fig. 5) are around 10 times primitive mantle for the HREE and
217 rise to 100 times for Rb and Ba, with Ce reaching 200-500 times primitive mantle. A
218 marked positive anomaly for Pb and K, and negative anomaly for Th and Ti are
219 present.

220 Relative to each other, the intermediate layer is the richest in incompatible
221 elements and thus likely to be more similar to a melt composition. The mafic boudin
222 is enriched in compatible elements such as Cr and Ni, and contains a similar amount
223 of HREE as the intermediate layer.

224

225 **5. Zircon U-Pb geochronology and trace element geochemistry**

226 The Pb-rich *HP* granulite (A1553) contains abundant zircon crystals which are
227 clear, colourless to light pink and generally euhedral, with dimension varying from
228 100 to 500 μm in length. The zircon internal structure is characterised by large cores
229 containing composite growth domains. Microstructurally, the youngest components in
230 the cores are large areas with broad-banded oscillatory-zoning (Fig. 6). Cores with
231 low CL emission and patchy zoning, likely to indicate metamictization, are also
232 present. The zircon cores commonly contain sealed fractures or deformation
233 structures as described in mylonitic rocks (Kaczmarek et al., 2008; Reddy et al.,
234 2006). Thin, unzoned rims are present in numerous crystals but only occasionally
235 reach a size that is suitable for SHRIMP analysis (20 μm).

236 SHRIMP analyses were concentrated on the texturally younger parts of the cores
237 and on the unzoned rims. Core apparent ages scatter along *Concordia* between \sim 500
238 and 350 Ma with a consistent group of the five oldest analyses defining a *Concordia*
239 age of 486 ± 7 Ma (Fig. 7).

240 The 18 analyses on rims yielded Pb-rich ages (Table 2) that, with the
241 exception of two, define a *Concordia* age of 340.7 ± 4.2 Ma (Fig. 7). Two analyses are
242 statistically younger and are suspected of Pb loss. Notably, the youngest analysis on
243 a zircon core is within error of the age of the rims.

244 Core and rim domains are distinct on the basis of their chemical composition
245 (Tables 2 and 3). There is significant overlapping in U contents between the two
246 domains, but the cores are generally richer in Th, resulting in higher Th/U (>0.3).
247 Cores are richer in REE and have a strong enrichment in HREE, whereas the rims
248 have a generally flat HREE pattern at 10-100 times chondrite (Fig. 8). Rims also have
249 a small negative or absent Eu anomaly, whereas the cores have a marked negative
250 Eu anomaly ($\text{Eu}/\text{Eu}^* < 0.4$).

251 Ti contents in the cores vary between 5 and 17 ppm (Table 3), which translate in
252 temperatures between 690-790 °C (Watson and Harrison, 2005). Zircon rims show
253 restricted variations in Ti content with respective temperatures of 710-770 °C. Such
254 temperatures are assuming rutile to be the buffering Ti phase, whereas T would be
255 ~ 50 °C higher if zircon grew in a titanite or ilmenite-bearing assemblage. In this
256 sample, rutile is the stable Ti-phase during *HP* metamorphism (stage A-B of Fig. 4,
257 Ferrando et al., 2008), and reacted to form titanite and then ilmenite during
258 decompression (stage C-D of Fig. 4, Ferrando et al., 2008).

259 The zircon cores in this Pl-rich *HP* granulite contain inclusions of plagioclase,
260 biotite, amphibole with composition similar to that found in basic layers (Ferrando et
261 al., 2008), and chlorite, phengite, apatite, quartz, rare rutile and K-feldspar.
262 However, these mineral inclusions are only contained in the cores and commonly
263 along fractures (Fig. 6). We interpret the inclusion assemblages as the combination
264 of inherited and secondary minerals that offer no insight on the condition of zircon
265 crystallization. Notably, no inclusion is contained in the ~ 340 Ma rims.

266

267 The Pl-poor *HP* granulite is relatively poor in zircon compared to its Pl-rich
268 counterpart. The zircons are clear, pink to light red in colour, and commonly have a
269 rounded shape. Their size is comparable to the other sample with diameters of 100-
270 500 μm . The internal structure is somewhat simpler, with most grains having
271 concentric broad-banded and sector zoning (Fig. 6). Fractures and deformation
272 features are present in about 50% of the grains. In several grains, thin bright rims
273 surround the cores, but only in a few cases their size allowed location of the ion
274 beam.

275 The zircon cores with sector zoning yielded ages between ~ 346 and 320 Ma, with
276 three rim analyses returning ages in the middle of this range. Cumulatively these

277 analyses define a Concordia age of 336.3 ± 4.1 Ma, excluding two statistically younger
278 analyses (Fig. 7). Out of the few texturally older cores, which have a different CL
279 zoning pattern, a single one was analysed and yielded a discordant $^{206}\text{Pb}/^{238}\text{U}$ age of
280 378 ± 6 Ma (Table 2).

281 The zircons contain amounts of U variable over more than an order of magnitude,
282 with the rims having the lowest concentrations. Th is generally low and $\text{Th}/\text{U} < 0.15$.
283 For the cores, REE patterns are enriched in HREE with respect to the LREE and show
284 a moderate negative Eu anomaly (0.5-0.6, Fig. 8). In comparison, the zircon rims are
285 distinguished because they have the lowest REE concentrations, limited HREE
286 enrichment and a weak negative Eu anomaly (0.7-0.9).

287 Ti contents are between 6 and 11 ppm, with no measurable difference between
288 cores and rims (Table 3). Ti-in-zircon thermometry (Watson and Harrison, 2005)
289 returns T of 700-750°C. This is again assuming formation in a rutile-bearing
290 assemblage with $T \sim 50^\circ\text{C}$ higher if zircon grew during decompression when ilmenite
291 was likely to be stable (Ferrando et al., 2008). Since the sample contains only rare
292 quartz the activity of SiO_2 may have been < 1 . Lower SiO_2 activity will shift calculated
293 temperatures toward lower values (N. Tailby, personal communication).

294 Mineral inclusions of biotite and plagioclase are present in zircon grains that have
295 disturbed CL patterns with patchy alteration and fractures, or in cores of possible
296 inherited nature. This suggests that the inclusions are mainly secondary or inherited
297 and thus do not offer significant information for the age interpretation.

298

299 **6. Discussion**

300 **6.1. Chemistry and age of the protolith**

301 The bulk rock chemistry of the different layers varies significantly, indicating that
302 the layers either represent different stages of melt evolution or are due to cumulus.
303 The relative enrichment in the basic boudin of compatible elements such as Cr and
304 Ni, despite similar enrichment in incompatible elements, indicates that it is likely to
305 be a cumulate rather than a more primitive melt. Similarly, with respect to the Pl-
306 poor boudin, the Pl-rich layer is enriched in Si and Sr, but relatively low in
307 incompatible elements with respect to the intermediate layer, suggesting that its
308 protolith was a plagioclase cumulate rather than a more evolved melt. The
309 intermediate layer is taken as most similar to the initial liquid composition because of
310 its enrichment in incompatible elements and moderate Si content. The protolith of
311 this layer was likely to be between gabbro, for its Si content, and diorite for its
312 relatively high Al and low Mg, Fe and Ca. When compared to continental crust and
313 arc magmas (Fig. 5) the intermediate layer shares several trace element features
314 (strong Cs enrichment, Pb and K positive anomaly, Nb and Ta depletion, Zr and Hf
315 relative enrichment and Ti negative anomaly) with the continental crust.

316 In summary, the Frisson Lakes mafic sequence is likely derived from a mafic,
317 layered intrusion with Pl-rich and Pl-poor (Cpx-rich) cumulus layers. The parental
318 magma was gabbroic to dioritic in composition with a strong crustal component. The
319 presence of inherited magmatic zircon is in line with a mafic parental magma with
320 crustal affinity.

321

322 The zircon cores offer some insight into the age of the protolith of the HP
323 granulites. The texturally younger growth zone in the zircon cores shows oscillatory
324 zoning, it has uniform chemical composition (Fig. 8) but variable U-Pb ages. These
325 domains have signs of deformation and intense fracturing (Fig. 6), which have been
326 previously demonstrated to favour Pb loss (e.g. Reddy et al., 1999). During the

327 intense deformation, Pb could have easily diffused out of the crystal, whereas trace
328 elements, which are more compatible in zircon, were retained. This decoupling of Pb
329 and other elements has been extensively documented, for example, in inherited
330 zircons within ultra-HP rocks of the Dabie-Sulu terrain (Xia et al., 2009). The
331 relatively high Th/U ratio, the steep HREE pattern and the marked negative Eu-
332 anomaly measured in the zircon cores are common features of magmatic zircons
333 (Hoskin and Schaltegger, 2003; Rubatto, 2002). We thus suggest that the texturally
334 younger, and volumetrically dominant part of the zircon cores formed during
335 magmatic crystallization of the protolith. The U-Pb system of these cores was partly
336 reset during the intense deformation associated with Variscan metamorphism (see
337 Section 6.2.). In such a scenario, the minimum age for the crystallization of the
338 magmatic zircon cores is constrained by the oldest ages measured in such domains,
339 i.e. 486 ± 7 Ma. The presence of metamorphic mineral inclusions in the zircon cores
340 (e.g. rutile) apparently contradicts this conclusion. However, the fact that such
341 inclusions occur mainly along fractures and deformation features makes their
342 petrological significance dubious.

343 Mafic magmas of Cambro-Ordovician age are reported across the External
344 Crystalline Massifs. The most prominent in size is the Chamrousse ophiolite
345 (Belledonne Massif, ~ 150 km NNW of the Argentera Massif), which formed at 496 ± 6
346 Ma in a back-arc basin (Ménot et al., 1988). The Chamrousse ophiolite is largely
347 composed of ocean floor tholeiites that are only marginally enriched in LREE and lack
348 the prominent crustal signature seen in the Frisson Lakes rocks (Bodinier et al.,
349 1982). Other Ordovician mafic rocks are disseminated within the External Crystalline
350 Massifs (Guillot and Menot, 2009; Ménot and Paquette, 1993; Rubatto et al., 2001),
351 occur as relatively small bodies within the crustal basement, are often associated
352 with Si-rich magmas, and are generally overprinted by high-grade metamorphism.

353 Their age varies between ~ 480 and 460 Ma and, similarly to the Frisson Lakes mafic
354 sequence, they show high degree of crustal contamination. This Ordovician bimodal
355 magmatism related to rifting is also known in the Massif Central (e.g. Pin and Marini,
356 1993) and is widespread in the Bohemian Massif, where it appears to be somewhat
357 older (~ 500 Ma, e.g. Turniak et al., 2000). In our opinion, the chemical features of
358 the Frisson Lakes mafic sequence can be better reconciled with those of this
359 Ordovician bimodal magmatism (Bodinier et al., 1982; Guillot and Menot, 2009), of
360 which the Frisson Lakes sequence would represent an early stage.

361

362 **6.2. Age and conditions of metamorphism**

363 Zircon rims in the PI-rich *HP* granulite and sector zoned domains in the PI-poor *HP*
364 granulite yielded indistinguishable Carboniferous ages at ~ 340 Ma (340.7 ± 4.2 and
365 336.3 ± 4.1 Ma, respectively). The low Th/U of the zircon rims in the PI-rich *HP*
366 granulite is a common feature of metamorphic zircon and can be ascribed to the
367 formation of a Th-rich phase such as monazite, which is abundant in this sample.
368 The HREE depletion in the zircon rims is in line with formation, before or during
369 zircon crystallization, of metamorphic garnet that sequestered HREE from the
370 reactive rock bulk (Rubatto, 2002). The zircon rims lack a significant negative Eu
371 anomaly, which is also absent in the other metamorphic minerals such as omphacite,
372 garnet and plagioclase (own unpublished data). Ti-in zircon thermometry indicates
373 temperatures of at least 700 - 770°C , which are within that reported for the *HP* peak
374 ($735 \pm 15^\circ\text{C}$, Ferrando et al., 2008) but generally higher than those of the first
375 retrogression stage ($709 \pm 2^\circ\text{C}$, Ferrando et al., 2008). All these chemical features are
376 interpreted to indicate zircon rim formation during *HP* granulite-facies
377 metamorphism.

378 Notably, the calculated Y and HREE partitioning between the ~340 zircon rims
379 and garnet, which has little zoning, returns values far lower than any published
380 equilibrium partitioning (Rubatto and Hermann, 2007). This suggests that the dated
381 zircon rims, despite having formed in an environment depleted in HREE by garnet
382 growth, are not in chemical equilibrium with the garnet now present in the rock. In
383 fact, textural relationships and chemical data (Ferrando et al., 2008) indicate that,
384 particularly in the Pl-rich granulite, garnet completely re-equilibrated during mylonitic
385 deformation (stage C in Fig. 4). Thus, the trace element disequilibrium between
386 zircon and mylonitic garnet supports zircon formation before the mylonitic overprint.
387 This example demands caution when applying partition coefficients in poorly
388 equilibrated and complex assemblages.

389 The zircons from the Pl-poor *HP* granulite A1554 have sector zoning that is not
390 particularly diagnostic: similar zoning has been described for granulite-facies zircon
391 (e.g. Vavra et al., 1996) as well as for gabbroic zircon (e.g. Rubatto and Gebauer,
392 2000). Despite their low Th/U, the REE patterns of the zircon from the Pl-poor *HP*
393 granulite resemble that of the magmatic zircon cores in the Pl-rich *HP* granulite (e.g.
394 HREE enrichment). HREE depletion would be expected in metamorphic zircon formed
395 in such a garnet-rich rock. Garnet in the sample has, in fact, a flat HREE pattern at
396 50-100 chondrite (own unpublished data). The few unzoned zircon rims in the Pl-
397 poor *HP* granulite that could be analysed show a distinctly lower HREE content, but
398 their age is undistinguishable, at this level of precision, from that of the cores. This
399 leads to the suggestion that the lack of HREE depletion in most of the metamorphic
400 zircons may be explained by delay in the growth of garnet in this rock. The
401 undistinguishable age between the zircon cores in the Pl-poor *HP* granulite and the
402 metamorphic zircon rims in the Pl-rich *HP* granulite forces a common interpretation,

403 i.e. they are both metamorphic despite the inconclusive features of the PI-poor *HP*
404 granulite zircons.

405 In the four-stage evolution reconstructed by Ferrando et al. (2008) for the Frisson
406 Lakes *HP* granulites (Fig. 4), it is concluded that the zircon rims formed before stage
407 C (mylonitisation at $665\pm 15^\circ\text{C}$ and 0.85 ± 0.15 GPa). This conclusion is based on the
408 intense deformation recorded by zircons and on the temperature given by the Ti-in-
409 zircon thermometry for the PI-rich sample. The regional anatexis post-dates both the
410 mylonitic stage and the intrusion of monzonites dated at 332 ± 3 Ma, which
411 underwent partial melting (Rubatto et al., 2001). This evolution is testified by the
412 discordant relationships between the mylonitic foliation of the *HP* granulite and the
413 hosting migmatitic granitoid gneiss, which preserves relicts of igneous fabric. This
414 leaves a window at $\sim 800\text{-}700^\circ\text{C}$ and $\sim 1.4\text{-}1.0$ GPa between the metamorphic peak
415 and the first decompression stage for the growth of the ~ 340 Ma zircon (Fig. 4).

416 The Frisson Lakes *HP* granulites essentially underwent the same metamorphic
417 evolution as the Meris eclogite (Ferrando et al., 2008), which recorded a different
418 assemblage simply because of its composition. We can therefore infer that ~ 340 Ma
419 also dates the metamorphic peak or early decompression in the eclogite. This
420 represents the first geochronological data on *HP* metamorphism in the Argentera
421 Massif and in the External Crystalline Massifs.

422

423 **6.3. Carboniferous *HP* metamorphism in the Variscan belt**

424 There are few and weak constraints on the age on *HP* metamorphism across the
425 European Variscan basement, particularly in its western part. This is largely due to
426 the poor preservation of *HP* assemblages, which were extensively retrogressed
427 during late-Variscan *HT* metamorphism and anatexis (von Raumer et al., 2009). The
428 pioneering zircon isotope-dilution TIMS work of Paquette et al. (1989) analysed mafic

429 rocks with variably preserved *HP* assemblages from eclogites (Belledonne and
430 Aiguilles Rouges Massifs) to garnet amphibolites (Argentera Massif). They obtained
431 mainly discordant data, whose upper and lower intercepts are of difficult
432 interpretation. In most samples, no age constraints on the *HP* metamorphism were
433 obtained, but for the Argentera Massif a lower intercept of 424 ± 4 Ma from an
434 amphibolite was proposed as the age of *HP* metamorphism. Notably, a second mafic
435 rock from the same area returned an upper intercept at ~ 350 Ma with a meaningless
436 lower intercept.

437 In Sardinia, at the southern end of the Variscan belt, a recent detailed study of
438 zircon from retrogressed eclogites failed to constrain the age of *HP* metamorphism,
439 but proposed an age of 352 ± 3 Ma for amphibolite-facies decompression after *HP*
440 metamorphism (Giacomini et al., 2005). An age of ~ 400 Ma has been speculated by
441 many authors for the Sardinia eclogites on the basis of poorly constrained zircon
442 data, whose relationship to *HP* metamorphism has, however, not been proven
443 (Cortesogno et al., 2004; Palmeri et al., 2004).

444 No other modern geochronology of eclogites has been carried out on the
445 Southern European Variscan belt and the age of Variscan eclogites remains unclear
446 in the western part of the Variscan orogeny. In the central Variscan, a hypothetical
447 460-470 Ma *HP* metamorphism was postulated on the basis of U-Pb and Sm-Nd
448 geochronology (Gebauer, 1993) in the Gotthard Massif. Further to the east, Sm-Nd
449 geochronology of eclogitic assemblages from the Eastern Alps returned younger ages
450 around 360-350 Ma for the Ötztal eclogites (Miller and Thöni, 1995) and ~ 330 Ma for
451 the *HP* rocks in the Ulten zone (Tumiati et al., 2003). Such ages are closer to the
452 more robust constraints on the age of Variscan *HP* metamorphism, which comes
453 from the Bohemian Massif, including the Polish Sudetes (Bröcker et al., 2009; Kröner
454 et al., 2000; Schulmann et al., 2005). SHRIMP U-Pb analyses on zircon within an *HP*

455 paragenesis returned ages of ~340 Ma (Kröner et al., 2000). This age was later
456 confirmed with Pb-evaporation analysis of zircon from an *HP* granulite (Schulmann et
457 al., 2005) and recent SHRIMP dating of zircon within a mafic eclogite of the Sudetes
458 (Bröcker et al., 2009).

459

460 From regional reviews (Franke and Stein, 2000; O'Brien, 2000) it appears that,
461 across the dismantled European Variscan orogen and excluding the anomalous data
462 from the Gotthard Massif, there are relicts of two eclogitic events: an early one in the
463 Devonian (~400 Ma) and a later one in the Carboniferous ~350-340 Ma. O'Brien
464 (2000) concluded that the Devonian *HP* rocks are remnants of medium-temperatures
465 (eclogites and blueschists) subduction of an oceanic sequence, whose products were
466 then already exhumed by Late Devonian. A later subduction cycle involved different,
467 mostly continental rock associations that reached higher temperatures (900-1000°C)
468 and produced extensive felsic granulites (Tajcmanova et al., 2006). For this second
469 Variscan subduction, O'Brien (2000) reported a likely age of ~340 Ma, based on data
470 from the Bohemian Massif. Subduction was followed by rapid exhumation and cross
471 cutting granite intrusions at 315–325 Ma, both contributing to the high thermal
472 gradient that led to widespread Variscan Barrovian metamorphism dated between
473 340 and 310 Ma in different regions (see below).

474 The continental nature of the protolith, the metamorphic grade, the rapid
475 decompression and age of the Frisson Lakes *HP* granulites ascribe these rocks to the
476 second subduction cycle. To our knowledge there is no relict of the Devonian,
477 medium temperature eclogites in the Argentera Massif or any of the External
478 Crystalline Massifs.

479

480 **6.4. Comparison with the Bohemian Massif and implications for**
481 **tectonic style**

482 These new results combined with previous data constrain the evolution of the
483 Gesso-Stura Terrain within the Argentera Massif before and during the Variscan
484 orogeny. Such evolution is likely to be largely comparable to that of other External
485 Crystalline Massifs, which show similar lithostratigraphy and metamorphic
486 assemblages (von Raumer et al., 2009).

487 Bimodal magmatism occurred in Ordovician to Silurian times with intrusion of
488 dacite and gabbros (Rubatto et al., 2001) in an already metamorphosed basement.
489 The crustal contamination in the Frisson Lakes mafic sequence supports an
490 extensional setting in agreement with what proposed for the External Crystalline
491 Massifs (Guillot and Menot, 2009; Ménot and Paquette, 1993). *HP* metamorphism at
492 the granulite-eclogite facies boundary occurred during the Carboniferous (~340-336
493 Ma) at conditions that could be compatible with subduction during continental
494 collision (e.g. O'Brien, 2000). The *HP* event was followed by limited magmatism of
495 likely extensional nature (intrusion of K-rich monzonites, Rubatto et al., 2001), with
496 extension being a likely cause of fast exhumation of the *HP* rocks. Shortly after, the
497 Massif underwent pervasive *LP-HT* metamorphism and anatexis (330-310 Ma Rubatto
498 et al., 2001). Carboniferous *HP* metamorphism in the Argentera Massif occurred only
499 some 10-20 Ma before the widespread migmatization documented not only in the
500 Massif but also elsewhere in the Variscan basement of Western Europe. The tight
501 succession of *HP* and *LP-HT* metamorphism suggests that the two stages are part of
502 the same metamorphic cycle where intense melting occurred upon decompression
503 and advective heat transfer. The final exhumation of the Massif is marked by the
504 unconformable deposition of Stephanian sediments (299-298 Ma, Faure-Muret,
505 1955).

506

507 In order to investigate the evolution of the Variscan orogen on a larger scale, a
508 comparison is attempted here with the Bohemian Massif, which is one of the largest
509 remnants of Variscan basement and occupies a strategic position at the eastern end
510 of Variscan Europe. This comparison is aided by the detailed tectonic and
511 geochronological constraints available for the Bohemian Massif, in comparison to
512 other portions of Variscan Europe.

513 The evolution of the Argentera Massif is similar, but not directly comparable in
514 age and metamorphic grade, to the evolution proposed for the Bohemian
515 counterpart (Kröner et al., 2000; Schulmann et al., 2009; Schulmann et al., 2005;
516 Tajcmanová et al., 2006). A significant difference is the presence in the Bohemian
517 Massif of medium temperature eclogites of presumably older age (~400-390 Ma)
518 that are taken to constrain Devonian subduction (see a review in O'Brien, 2000;
519 Schulmann et al., 2009). No evidence of such assemblages is present in the western
520 part of the Variscan orogen. The Sardinian eclogite of presumed ~400 Ma age
521 followed a high temperature path more similar to the Argentera *HP* granulite rocks.

522 Carboniferous collision in the Bohemian Massif produced thick continental roots.
523 Within this scenario, the Carboniferous *HP* assemblages in the felsic granulites
524 recorded higher metamorphic conditions of >15 kbar and >850-900 °C (Kröner et
525 al., 2000; Tajcmanová et al., 2006), which are not reported for the western Variscan
526 orogen. Two different geotherms have been proposed to explain contrasting, but
527 coeval metamorphic conditions recorded by felsic granulites and mafic eclogites in
528 the Bohemian Massif, (e.g. Konopásek and Schulmann, 2005; Štípská et al., 2006).
529 On the contrary, the Frisson Lakes *HP*-granulites and the Meris mafic eclogite within
530 the Argentera Massif record similar peak and exhumation conditions, as discussed in
531 detail by Ferrando et al. (2008). To our knowledge, no such duality of Carboniferous

532 *HP* metamorphism has been documented in other Variscan massifs. For the
533 Bohemian Massif, *HP* and ultra-*HP* metamorphism are generally attributed to
534 subduction, but an alternative model of accretionary prism above an underthrust
535 continental crust has been proposed for the *HP* granulites (e.g. Schulmann and
536 Gayer, 2000). This latter model is supported by the high geothermal gradient and
537 rapid progression to anatexis (Stípská et al., 2006). Such alternative settings remain
538 unexplored for the Argentera Massif.

539 A significant difference between the western and eastern Variscan is the age of
540 anatexis. In the south-east anatexis must be younger than ~330 Ma (Rubatto et al.,
541 2001) and likely between 320 and 310 Ma (Demoux et al., 2008; Rubatto et al.,
542 2001), and therefore delayed of 10-20 Ma after *HP* metamorphism. In the Bohemian
543 Massif, this time gap is not present as migmatisation occurred at ~340 Ma (e.g.
544 Anczkiewicz et al., 2007; Bröcker et al., 2009; Schulmann et al., 2005) during fast
545 decompression of the *HP* rock.

546 The differences between the eastern and western Variscan, which may be partly
547 attributed to poor preservation and limited data for the western units, are
548 nevertheless significant and attest to variation in timing and metamorphic conditions
549 along the axis of the vast Variscan orogen. Despite such differences, the eastern and
550 western portions of Variscan Europe show many intriguing similarities in their *P-T*-
551 time evolution (cf. *P-T*-time in this work and Tajcmanová et al., 2006).

552 The evolution proposed here for the Argentera Massif (Fig. 4) does not support an
553 Andean-style model as proposed by Schulmann et al. (2009) for the Bohemian
554 Massif. The major difference with the Andean model being the lack of both low-
555 medium temperature high-pressure rocks, and significant arc-related magmatism
556 during or after Carboniferous subduction. In the Argentera Massif, Carboniferous
557 alkaline magmas are small in volume and likely related to extension (monzonite at

558 332 Ma, Rubatto et al., 2001), with the possible exclusion of the mafics in the
559 Bousset-Valmasque Complex, which age is however unconstrained.

560 The new data also support the hypothesis that the overall evolution of the
561 Variscan belt resembles that of the Himalayan chain. Whereas this comparison has
562 been proposed for the eastern Variscan (Massonne and O'Brien, 2003; O'Brien, 2000;
563 Stípská et al., 2006), with the new data presented here it is possible to extend it to
564 the western Variscan. Similarities between the Variscan and the Himalayan orogenies
565 include the conditions of *HP* granulite-facies metamorphism, and the rapid
566 succession (within <20 Ma) of *HP* conditions, fast exhumation and widespread
567 anatexis.

568

569 **ACKNOWLEDGMENTS**

570 The Electron Microscopy Unit at ANU is thanked for access to the SEM facilities.
571 The constructive comments from D. A. Schneider and an anonymous reviewer helped
572 to improve the manuscript. D.R. acknowledges the financial support of the Australian
573 Research Council (DP0556700). R.C. and S.F. gratefully acknowledge the support of
574 the Italian Research Programmes of National Interest (P.R.I.N. Cofin 2004:
575 "Evolution of gondwanian and perigondwanian terranes in the Variscides of Western-
576 Central Alps and Sardinia-Corsica massif", Scientific Project Coordinator L.
577 Cortesogno).

578

579 **REFERENCES**

580 Anczkiewicz, R., Szczepanski, J., Mazur, S., Storey, C., Crowley, Q., Villa, I.M., Thirlwall, M.F.
581 and Jeffries, T.E., 2007. Lu-Hf geochronology and trace element distribution in
582 garnet: Implications for uplift and exhumation of ultra-high pressure granulites in the
583 Sudetes, SW Poland. *Lithos*, 95: 363-380.

584 Aranovich, L.Y. and Newton, R.C., 1996. H₂O activity in concentrated NaCl solutions at high
585 pressures and temperatures measured by the brucite-periclase equilibrium
586 *Contributions to Mineralogy and Petrology*, 125: 200-212.

587 Bierbrauer, K., 1995. Quantitative Verteilung von Deformation und Strukturen im
588 migmatischen Gesteinen der Mittel/Unterkruste. 3D- Strukturmodellierung im
589 kristallinen Argentera Massiv in der Externzone der Westalpen. PhD Thesis Thesis,
590 University of Würzburg, Germany, 225 pp.

591 Bigot-Cormier, F., Sosson, M., Poupeau, G., Stéphan, J.-F. and Labrin, E., 2006. The
592 denudation history of the Argentera Alpine External Crystalline Massif (Western Alps,
593 France-Italy): an overview from the analysis of fission tracks in apatites and zircons
594 *Geodinamica Acta*, 19: 455-473.

595 Black, L.P., Kamo, S.L., Allen, C.M., Aleinikoff, J.M., Davis, D.W., Korsch, R.J. and Foudoulis,
596 C., 2003. TEMORA 1: a new zircon standard for Phanerozoic U-Pb geochronology.
597 *Chemical Geology*, 200: 155-170.

598 Bodinier, J.L., Dupuy, C., Dostal, J. and Carme, F., 1982. Geochemistry of ophiolites from the
599 Chamrousse complex (Belledonne Massif, Alps). *Contributions to Mineralogy and*
600 *Petrology*, 78: 379-388.

601 Bröcker, M., Klemd, R., Cosca, M., Brock, W., Larionov, A.N. and Rodionov, N., 2009. The
602 timing of eclogite facies metamorphism and migmatization in the Orlica-Śnieżnik
603 complex, Bohemian Massif: Constraints from a multimethod geochronological study.
604 *Journal of Metamorphic Geology*, 27: 385-403.

605 Colombo, F., 1996. Evoluzione tettonico-metamorfica del Complesso Malinvern-Argentera
606 (Massiccio Cristallino dell'Argentera, Alpi Marittime, Italia), PhD Thesis, University of
607 Turin, Italy, Turin, 125 pp.

608 Colombo, F., Compagnoni, R. and Lombardo, B., 1994. Le rocce eclogitiche dei Laghi del
609 Frisson (Argentera sud-orientale, Alpi Marittime). *Atti Ticinesi di Scienze della Terra*,
610 *Serie Speciale*, 1: 75-82.

611 Corsini, M., Ruffet, G. and Caby, R., 2004. Alpine and late-hercynian geochronological
612 constraints in the Argentera Massif (Western Alps). *Eclogae Geologica Helvetica*, 97:
613 3-15.

614 Cortesogno, L., Gaggero, L., Oggiano, G. and Paquette, J.L., 2004. Different tectono-thermal
615 evolutionary paths in eclogitic rocks from the axial zone of the Variscan chain in
616 Sardinia (Italy) compared with the Ligurian Alps. *Ofioliti*, 29: 125-144.

617 Demoux, A., Scharer, U. and Corsini, M., 2008. Variscan evolution of the Tanneron massif, SE
618 France, examined through U-Pb monazite ages. *Journal of the Geological Society*,
619 165: 467-478.

620 Eggins, S.M., Rudnick, R.L. and McDonough, W.F., 1998. The composition of peridotites and
621 their minerals: a laser ablation ICP-MS study. *Earth and Planetary Science Letters*,
622 154: 53-71.

623 Faure-Muret, A., 1955. *Etudes géologiques sur le massif de l'Argentera-Mercantour et ses*
624 *enveloppes sédimentaires. Mémoires pour servir à l'explication de la Carte géologique*
625 *détaillée de la France*, Paris, France, 336 pp..

626 Ferrando, S., Lombardo, B. and Compagnoni, R., 2008. Metamorphic history of HP mafic
627 granulites from the Gesso-Stura Terrain (Argentera Massif, Western Alps, Italy).
628 *European Journal of Mineralogy*, 20: 777-790.

629 Ferrara, G. and Malaroda, R., 1969. Radiometric age of granitic rocks from the Argentera
630 Massif (Maritime Alps). *Bollettino della Società Geologica Italiana*, 88: 311-320.

631 Franke, W. and Stein, E., 2000. Exhumation of high-grade rocks in the Saxo-Thuringian Belt:
632 geological constraints and geodynamic concepts. In: W. Franke, V. Haak, O. Oncken
633 and D. Tanner (Editors), *Orogenic Processes: Quantification and Modelling in the*
634 *Variscan Belt*. The Geological Society, London, pp. 337-354.

635 Gebauer, D., 1993. The pre-Alpine evolution of the continental crust of the Central Alps - An
636 overview. In: J.F. von Raumer and F. Neubauer (Editors), *Pre-Mesozoic geology in*
637 *the Alps*. Springer, Berlin Heidelberg, pp. 93-117.

638 Giacomini, F., Bomparola, R.M. and Ghezzo, C., 2005. Petrology and geochronology of
639 metabasites with eclogite facies relics from NE Sardinia: constraints for the
640 Palaeozoic evolution of Southern Europe. *Lithos*, 82: 221-248.

641 Giacomini, F., Dallai, L., Carminati, E., Tiepolo, M. and Ghezzo, C., 2008. Exhumation of a
642 Variscan orogenic complex: insight into the composite granulitic-amphibolitic
643 metamorphic basement of south-east Corsica (France). *Journal of Metamorphic*
644 *Geology*, 26: 403-436.

645 Guillot, S. and Menot, R.P., 2009. Paleozoic evolution of the External Crystalline Massifs of the
646 Western Alps. *Comptes Rendus Geoscience*, 341: 253-265.

647 Holdaway, M.J. and Mukhopadhyay, B., 1993. A re-evaluation of the stability relations of
648 andalusite: thermochemical data and phase diagram for the aluminium silicates
649 *American Mineralogist*, 78: 298-315.

650 Hoskin, P.W.O. and Schaltegger, U., 2003. The composition of zircon and igneous and
651 metamorphic petrogenesis. In: J.M. Hanchar and P.W.O. Hoskin (Editors), *Zircon.*
652 *Reviews in Mineralogy and Geochemistry*. Mineralogical Society of America,
653 Washington, pp. 27-62.

654 Kaczmarek, M.-A., Müntener, O. and Rubatto, D., 2008. Trace element chemistry and U-Pb
655 dating of zircons from oceanic gabbros and their relationship with whole rock
656 composition (Lanzo, Italian Alps). *Contributions to Mineralogy and Petrology*, 155:
657 295-312.

658 Kelemen, P.B., Hanghøj, K. and Greene, A.R., 2004. One View of the Geochemistry of
659 Subduction-related Magmatic Arcs, with an Emphasis on Primitive Andesite and Lower
660 Crust In: R. Rudnick (Editor), *The crust Treatise on Geochemistry Elsevier*,
661 Amsterdam pp. 593-659.

662 Konopásek, J. and Schulmann, K., 2005. Contrasting Early Carboniferous field geotherms:
663 Evidence for accretion of a thickened orogenic root and subducted Saxothuringian
664 crust (Central European Variscides). *Journal of the Geological Society*, 162: 463-470.

665 Kröner, A., O'Brien, P.J., Nemchin, A.A. and Pidgeon, R.T., 2000. Zircon ages for high
666 pressure granulites from South Bohemia, Czech Republic, and their connection to
667 Carboniferous high temperature processes. *Contributions to Mineralogy and
668 Petrology*, 138: 127-142.

669 Ludwig, K.R., 2003. *Isoplot/Ex version 3.0. A geochronological toolkit for Microsoft Excel. 1a*,
670 Berkeley Geochronological Centre Spec. Pub., Berkeley.

671 Malaroda, R., Carraro, F., Dal Piaz, G.V., Franceschetti, B., Sturani, C. and Zanella, E., 1970.
672 Carta geologica del Massiccio dell'Argentera alla scala 1:50.000 e note illustrative.
673 *Memorie della Societa' Geologica Italiana*, 9: 557-663.

674 Massonne, H.J. and O'Brien, P.J., 2003. The Bohemian Massif and the NW Himalaya. In: D.A.
675 Carswell and R. Compagnoni (Editors), *Ultrahigh Pressure Metamorphism. EMU Notes
676 in Mineralogy*, Eötvös University Press, Budapest.

677 Matte, P., 2001. The Variscan collage and orogeny (480-290 Ma) and the tectonic definition
678 of the Armorica microplate: a review. *Terra Nova* 13: 122-128.

679 McDonough, W.F. and Sun, S.s., 1995. The composition of the Earth. *Chemical Geology*, 120:
680 223-253.

681 Ménot, R.P. and Paquette, J.L., 1993. Geodynamical significance of basic and bimodal
682 magmatism in the External Domains. In: J.F. von Raumer and F. Neubauer (Editors),
683 *Pre-Mesozoic geology in the Alps*. Springer Berlin, Heidelberg pp. 241-254.

684 Ménot, R.P., Pecaut, J.J., Scarenzi, D. and Piboule, M., 1988. 496 Ma age of plagiogranites in
685 the Chamrousse ophiolite complex (external crystalline massifs in the French Alps):
686 evidence of a Lower Palaeozoic oceanization. *Earth and Planetary Science Letters*, 88:
687 82-92.

688 Miller, C. and Thöni, M., 1995. Origin of eclogites from the Austroalpine Ötztal basement
689 (Tirol, Austria): geochemistry and Sm---Nd vs. Rb---Sr isotope systematics. *Chemical
690 Geology*, 122: 199-225.

691 Monié, P. and Maluski, H., 1983. Données géochronologiques ³⁹Ar-⁴⁰Ar sur le socle anté-
692 permien du massif de l'Argentera-Mercantour (Alpes-Maritimes, France). *Bullettin de
693 la Société géologique de France*, s. 7, 25: 247-257.

694 O'Brien, P.J., 2000. The fundamental Variscan problem: high-temperature metamorphism at
695 different depths and high-pressure metamorphism at different temperatures In: W.

696 Franke, V. Haak, O. Oncken and D. Tanner (Editors), *Orogenic Processes:*
697 *Quantification and Modelling in the Variscan Belt.* The Geological Society, London, pp.
698 369-386.

699 Palmeri, R., Fanning, M., Franceschelli, M., Memmi, I. and Ricci, C.A., 2004. SHRIMP dating of
700 zircons in eclogite from the Variscan basement in north-eastern Sardinia (Italy).
701 *Neues Jahrbuch für Mineralogie-Monatshefte*: 275-288.

702 Paquette, J.-L., Ménot, R.-P. and Pecaut, J.-J., 1989. REE, Sm-Nd and U-Pb zircon study of
703 eclogites from the Alpine External Massifs (Western Alps): evidence for crustal
704 contamination. *Earth and Planetary Science Letters*, 96: 181-198.

705 Pin, C. and Marini, F., 1993. Early Ordovician continental break-up in Variscan Europe: NdSr
706 isotope and trace element evidence from bimodal igneous associations of the
707 Southern Massif Central, France. *Lithos*, 29: 177-196.

708 Reddy, S.M., Timms, N.E., Trimby, P., Kinny, P.D., Buchan, C. and Blake, k., 2006. Crystal-
709 plastic deformation of zircon: A defect in the assumption of chemical robustness.
710 *Gelogy*, 34: 257-260.

711 Reddy, S.M., Wheeler, J. and Cliff, R., 1999. The geometry and timing of orogenic extension:
712 an example from the Western Italian Alps. *Journal of Metamorphic Geology*, 17: 573-
713 589.

714 Rubatto, D., 2002. Zircon trace element geochemistry: distribution coefficients and the link
715 between U-Pb ages and metamorphism. *Chemical Geology*, 184: 123-138.

716 Rubatto, D. and Gebauer, D., 2000. Use of cathodoluminescence for U-Pb zircon dating by
717 ion microprobe: some examples from the Western Alps. In: M. Pagel, V. Barbin, P.
718 Blanc and D. Ohnenstetter (Editors), *Cathodoluminescence in geosciences.* Springer,
719 Berlin Heidelberg New York, pp. 373-400.

720 Rubatto, D. and Hermann, J., 2007. Experimental zircon/melt and zircon/garnet trace
721 element partitioning and implications for the geochronology of crustal rocks.
722 *Chemical Geology*, 241: 62-87.

723 Rubatto, D., Schaltegger, U., Lombardo, B. and Compagnoni, R., 2001. Complex Paleozoic
724 magmatic and metamorphic evolution in the Argentera Massif (Western Alps)
725 resolved with U-Pb dating. *Schweizerische Mineralogische und Petrographische*
726 *Mitteilungen*, 81: 213-228.

727 Rudnick, R. and Gao, S., 2004. Composition of the Continental Crust. In: R. Rudnick (Editor),
728 *The crust. Treatise on Geochemistry*, Elsevier, Amsterdam, pp. 1-64.

729 Schulmann, K. and Gayer, R., 2000. A model for a continental accretionary wedge developed
730 by oblique collision: The NE Bohemian Massif. *Journal of the Geological Society*, 157:
731 401-416.

732 Schulmann, K., Konopásek, J., Janousek, V., Lexa, O., Lardeaux, J.-M., Edel, J.-B., Stípská, P.
733 and Ulrich, S., 2009. An Andean type Palaeozoic convergence in the Bohemian
734 Massif. *Comptes Rendus Geosciences*, 341: 266-286.

735 Schulmann, K., Kröner, A., Hegner, E., Wendt, I., Konopásek, J., Lexa, O. and Stípská, P.,
736 2005. Chronological constraints on the pre-orogenic history, burial and exhumation of
737 deep-seated rocks along the eastern margin of the Variscan Orogen, Bohemian
738 Massif, Czech Republic. *American Journal of Science*, 305: 407-448.

739 Stacey, J.S. and Kramers, J.D., 1975. Approximation of terrestrial lead evolution by a two-
740 stage model. *Earth and Planetary Science Letters*, 26: 207-221.

741 Stampfli, G.M., von Raumer, J.F. and Borel, G.D., 2002. Paleozoic evolution of pre-Variscan
742 terranes: from Gondwana to the Variscan collision. *Geological Society of America*
743 *Special Paper*, 364: 263-280.

744 Štípská, P., Pitra, P. and Powell, R., 2006. Separate or shared metamorphic histories of
745 eclogites and surrounding rocks? An example from the Bohemian Massif. *Journal of*
746 *Metamorphic Geology*, 24: 219-240.

747 Tajcmanová, L., Konopásek, J. and Schulmann, K., 2006. Thermal evolution of the orogenic
748 lower crust during exhumation within a thickened Moldanubian root of the Variscan
749 belt of Central Europe. *Journal of Metamorphic Geology*, 24: 119-134.

750 Tumati, S., Thöni, M., Nimis, P., Martin, S. and Mair, V., 2003. Mantle-crust interactions
751 during Variscan subduction in the Eastern Alps (Nonsberg-Ulten zone):
752 Geochronology and new petrological constraints. *Earth and Planetary Science Letters*,
753 210: 509-526.

754 Turniak, K., Mazur, S. and Wysoczanski, R., 2000. SHRIMP zircon geochronology and
755 geochemistry in the Orlica-Snieznick gneisses (Variscan belt of Central Europe) and
756 their tectonic implications. *Geodinamica Acta*, 13: 293-312.

757 Vavra, G., Gebauer, D., Schmidt, R. and Compston, W., 1996. Multiple zircon growth and
758 recrystallization during polyphase Late Carboniferous to Triassic metamorphism in
759 granulites of the Ivrea Zone (Southern Alps): an ion microprobe (SHRIMP) study.
760 *Contributions to Mineralogy and Petrology*, 122: 337-358.

761 von Raumer, J.F. and Bussy, F., 2004. Mont Blanc and Aiguilles Rouges: Geology of their
762 polymetamorphic basement (External Massifs, Western Alps, France-Switzerland).
763 *Mémoires de Géologie*, 42: 1-204.

764 von Raumer, J.r.F., Bussy, F. and Stampfli, G.M., 2009. The Variscan evolution in the External
765 Massifs of the Alps and place in their Variscan framework. *Comptes Rendus*
766 *Geosciences*, 341: 239-252.

767 Watson, E.B. and Harrison, T.M., 2005. Zircon thermometer reveals minimum melting
768 conditions on earliest Earth. *Science*, 308: 841-844.

- 769 Williams, I.S., 1998. U-Th-Pb geochronology by ion microprobe. In: M.A. McKibben, W.C.
770 Shanks III and W.I. Ridley (Editors), Application of microanalytical techniques to
771 understanding mineralizing processes. Reviews in Economic Geology, Society of
772 Economic Geologists, pp. 1-35.
- 773 Xia, Q.X., Zheng, Y.F., Yuan, H. and Wu, F.Y., 2009. Contrasting Lu-Hf and U-Th-Pb isotope
774 systematics between metamorphic growth and recrystallization of zircon from
775 eclogite-facies metagranites in the Dabie orogen, China. Lithos, 112: 477-496
776

777 **FIGURES and TABLES CAPTIONS**

778

779 Table 1. XRF bulk rock chemical analyses.

780 Table 2. SHRIMP U-Pb analyses of zircons.

781 Table 3. LA-ICPMS analyses of zircons.

782

783

784 Fig. 1. a) Map of the European Variscan orogen (modified from O'Brien, 2000;
785 Stampfli et al., 2002; von Raumer and Bussy, 2004). C: Corsica; MT: Maures-
786 Tanneron Massif; RH: Rheno-Hercynian; S: Sardinia; SW: Schwarzwald; V: Vosges.
787 The Argentera Massif is shown in the box. b) Geological sketch of the Argentera
788 Massif. The samples were collected at Frisson Lakes, indicated with a star.

789

790 Fig. 2. Geological sketch-map of the Frisson Lakes area (modified after
791 Colombo et al., 1994).

792

793 Fig. 3. a) Field occurrence of the Frisson Lakes mafic sequence with alternating
794 layers of PI-poor and PI-rich (similar to sample A1553) *HP* granulites. Sample A1554
795 correspond to the dark boudin. b) Scan of a thin section of PI-rich *HP* granulite
796 A1553 illustrating the mylonitic texture with relict garnet porphyroclasts. Field of
797 view: 2.0x1.75 cm. c) Scan of a thin section of PI-poor *HP* granulite (sample A1554)
798 with a cataclastic texture defined by large garnet crystals within a matrix mainly
799 composed of clinopyroxene, amphibole and minor plagioclase. Field of view: 2.3x1.9
800 cm.

801

802 Fig. 4. *P-T*-time evolution of the Gesso-Stura Terrain. Phase relations for
803 Al_2SiO_5 are after Holdaway & Mukhopadhyay (1993) and the wet granite solidus is
804 after Aranovich & Newton (Aranovich and Newton, 1996). *P-T* conditions for stages
805 A-D (ellipses) are from Ferrando et al. (2008) and for the anatexis (cross) are from
806 Bierbrauer (1995). Geochronological data are from this work, (1) Rubatto et al.
807 (2001) and (2) Faure-Muret (1955).

808

809 Fig. 5. Primitive mantle normalized diagram of bulk rock chemical
810 compositions. Normalizing values according to McDonough and Sun (1995). Mariana
811 Arc composition from Kelemen et al. (2004) and upper crust composition from
812 Rudnick and Gao (2004).

813

814 Fig. 6. Cathodoluminescence images of zircon crystals from the two samples.
815 Dotted circles indicate LA-ICP-MS analyses for trace elements, and small circles
816 indicate SHRIMP analyses for U-Pb. For each SHRIMP analysis, ages are given in
817 $\text{Ma} \pm 1$ sigma. Scale bar represents 100 μm . Note the large inherited cores in the Pl-
818 rich HP granulite A1553, which yield scattering ages. The linear features cutting
819 across the crystal are due to deformation. See text for discussion.

820

821 Fig. 7. *Concordia* plots for SHRIMP U-Pb analyses. Data were corrected for
822 common Pb. Ellipses are 2 sigma errors. Dotted ellipses are excluded from the
823 *Concordia* age calculation. See text for discussion.

824

825 Fig. 8. Chondrite normalized trace element pattern of zircons from the dated
826 samples (A1553 and A1554). Normalizing values according to McDonough and Sun
827 (1995). See text for discussion.

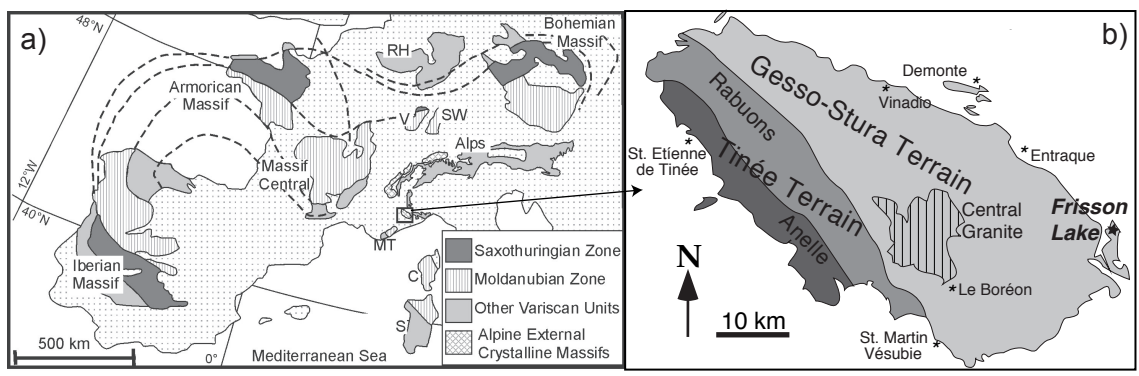

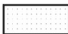









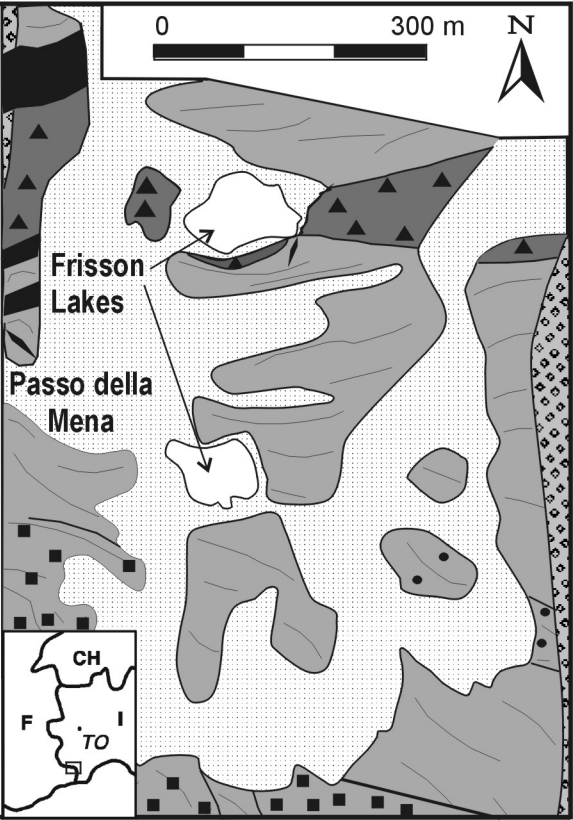
Figure 1.

Legend

-  Fault
-  Quaternary deposits
-  Alpine mylonite
-  Permian sandstone and conglomerate
-  Aplite dyke
-  Migmatitic paragneiss
-  Amphibole migmatite
-  Migmatitic granitoid gneiss
-  Frisson Lakes mafic sequence

0 300 m

N



Frisson Lakes

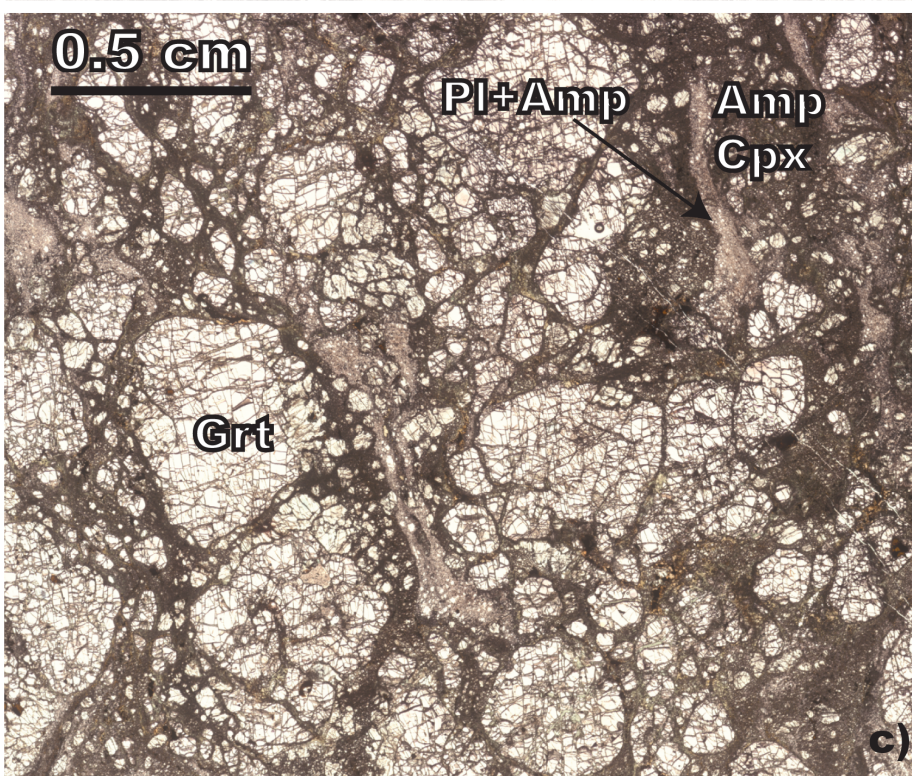
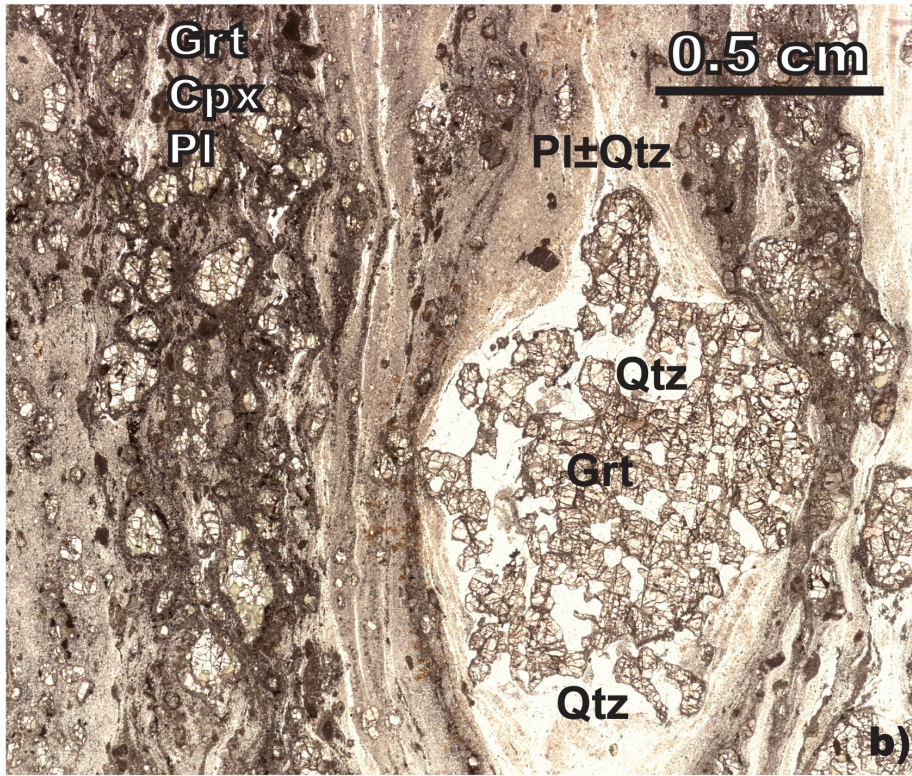
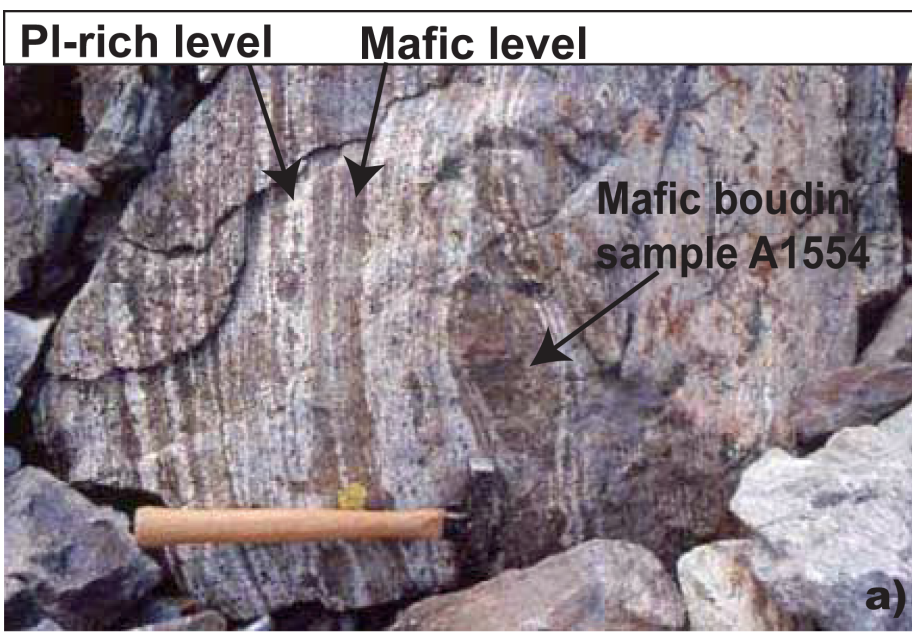
Passo della Mena

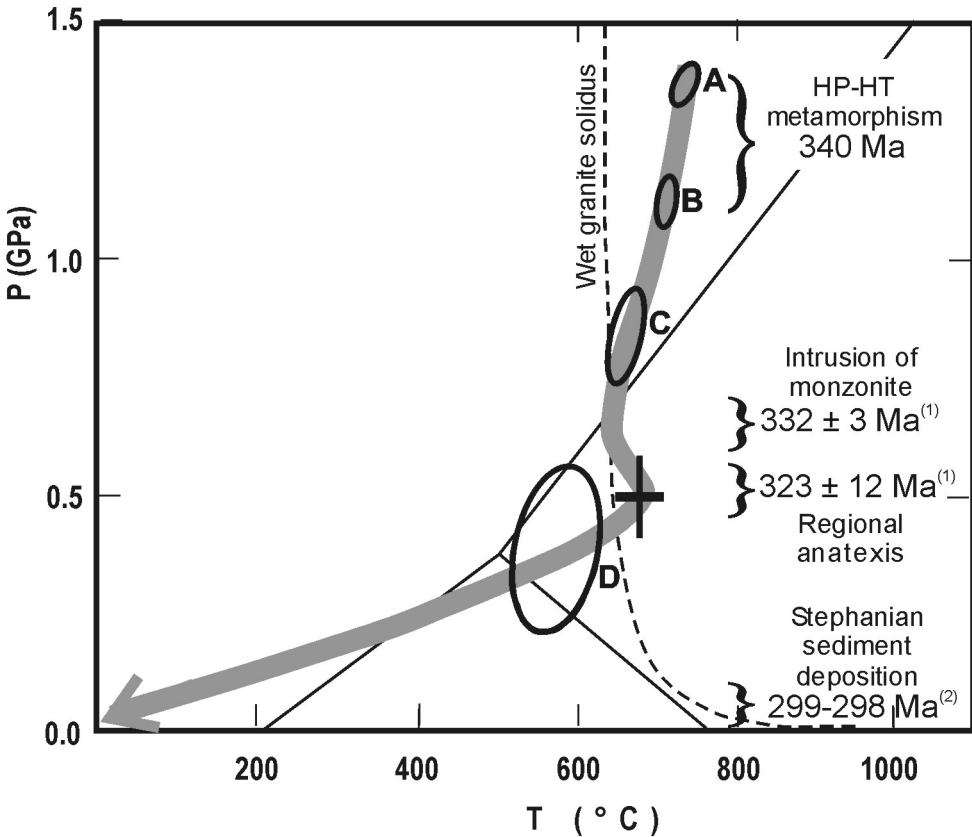
CH

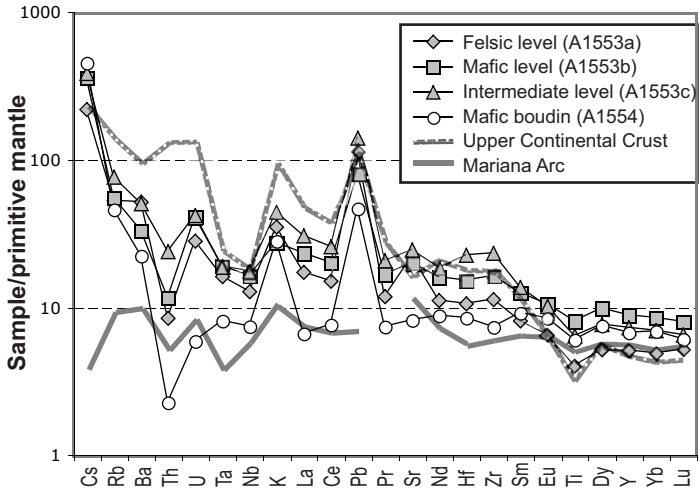
F

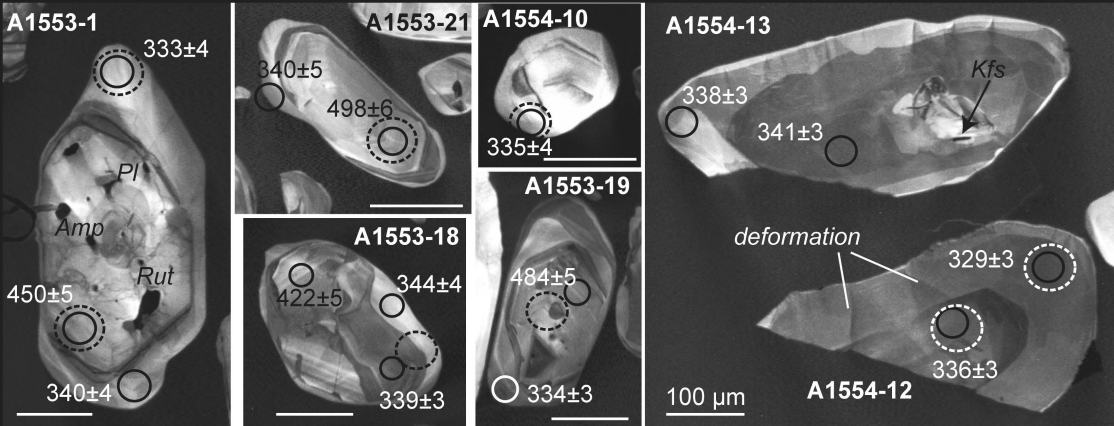
TO

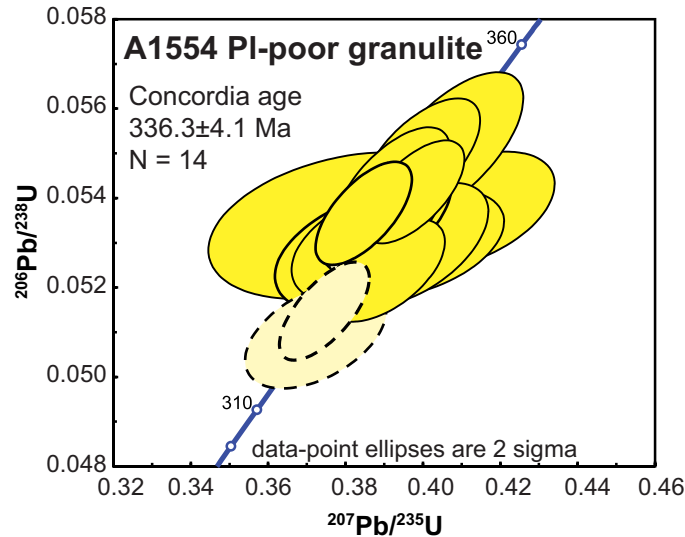
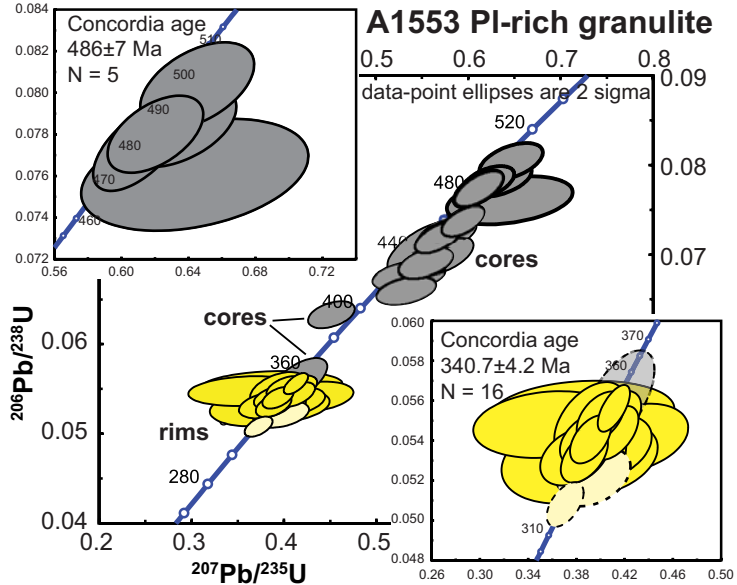
I











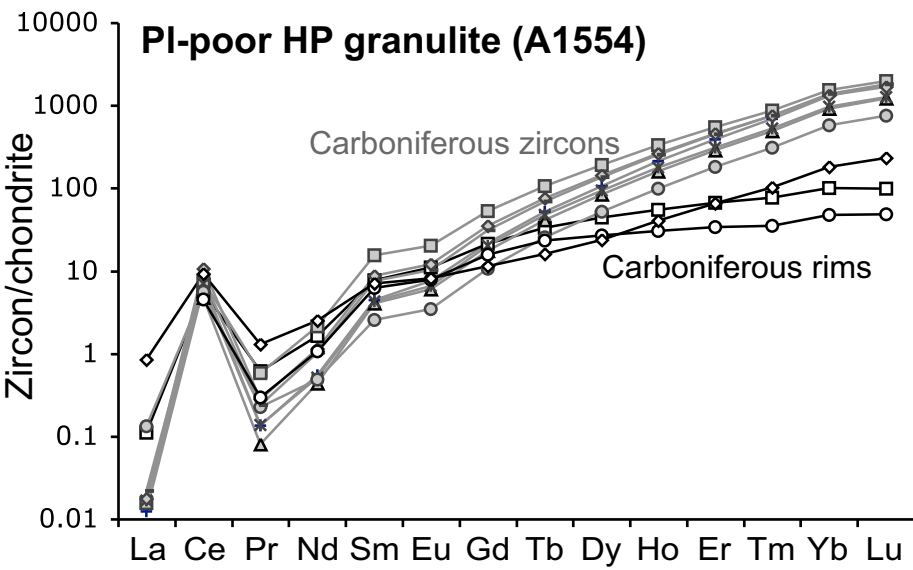
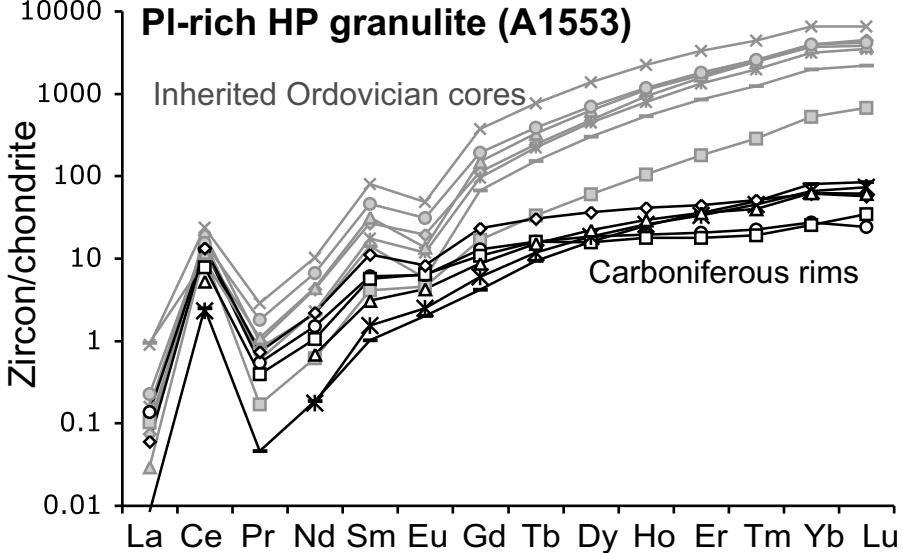


TABLE 1. XRF bulk rock analyses.

	A1553a	A1553c	A1553b	A1554
	wt % felsic layer	intermediate layer	basic layer	mafic boudin
SiO ₂	56.10	51.70	49.50	45.80
Al ₂ O ₃	17.95	18.25	16.35	16.45
FeO	5.13	6.62	8.84	8.31
Fe ₂ O ₃	1.30	1.64	1.87	3.26
CaO	5.89	6.69	7.48	10.25
MgO	3.95	4.94	5.86	9.43
Na ₂ O	5.88	4.50	3.39	2.48
K ₂ O	1.02	1.29	0.80	0.82
Cr ₂ O ₃	0.01	0.02	0.02	0.04
TiO ₂	0.81	1.29	1.62	1.21
MnO	0.10	0.13	0.19	0.19
P ₂ O ₅	0.16	0.32	0.33	0.12
SrO	0.05	0.06	0.05	0.02
BaO	0.04	0.04	0.02	0.02
LOI	1.10	1.67	1.45	1.32
Total	100.00	99.90	98.80	100.50
Mg#	0.435	0.427	0.399	0.532
	ppm			
Ag	<1	<1	<1	<1
Ba	341	333	218	147.5
Ce	25.2	43.1	33.6	12.8
Co	20.0	26.3	35.4	46.5
Cr	120	120	150	290
Cs	4.59	8.05	7.50	9.48
Cu	23.0	29.0	39.0	43.0
Dy	3.48	5.17	6.64	5.06
Er	2.30	3.14	4.14	3.14
Eu	1.00	1.56	1.62	1.30
Ga	19.5	23.8	22.2	18.9
Gd	3.32	5.58	5.68	4.36
Hf	3.00	6.40	4.30	2.40
Ho	0.69	1.04	1.34	1.02
La	11.2	19.8	15.1	4.3
Lu	0.35	0.44	0.54	0.41
Mo	<2	<2	<2	<2
Nb	8.40	11.6	10.8	4.90
Nd	13.9	23.2	20.0	11.0
Ni	41.0	47.0	54.0	116
Pb	17.0	21.0	12.0	7.0
Pr	3.01	5.24	4.23	1.88
Rb	31.7	45.8	33.2	27.5
Sm	3.29	5.54	5.09	3.72
Sn	2.0	4.0	3.0	3.0
Sr	440	486	399	163
Ta	0.6	0.7	0.7	0.3
Tb	0.55	0.91	1.04	0.8
Th	0.67	1.9	0.92	0.18
Tl	<0.5	<0.5	<0.5	<0.5
Tm	0.30	0.44	0.55	0.43
U	0.57	0.85	0.83	0.12
V	116	160	222	243
W	1.0	1.0	2.0	2.0
Y	22.0	31.3	38.1	29.0
Yb	2.15	3.06	3.74	3.04
Zn	85	112	129	122
Zr	119	244	172	77

Table 2. SHRIMP U-Pb analyses of zircons.

Label	CL domain	Pb _c % U (ppm)	Th (ppm)	Th/U	²⁰⁶ Pb/ ²³⁸ U Age	±1 sigma	²⁰⁶ Pb/ ²³⁸ U	±1 sigma	²⁰⁷ Pb/ ²³⁵ U	% error (1 sigma)	²⁰⁶ Pb/ ²³⁸ U	% error (1 sigma)	error correlation	
Felsic granulite (A1553)														
A1553-9.1	rim	0.06	470	9	0.02	319.5	2.8	0.05081	0.00046	0.3699	1.70	0.05081	0.90	0.526
A1553-7.1	rim	0.00	94	54	0.59	327.9	4.1	0.05219	0.00067	0.3945	3.12	0.05219	1.14	0.366
A1553-1.1	rim	0.11	111	5	0.05	332.7	4.2	0.05296	0.00069	0.3913	3.10	0.05296	1.30	0.419
A1553-11.1	rim light	0.13	54	19	0.36	333.5	4.8	0.05309	0.00078	0.4047	4.31	0.05309	1.38	0.319
A1553-15.1	rim light	0.95	31	18	0.60	333.5	6.4	0.05310	0.00105	0.3791	6.74	0.05310	1.72	0.255
A1553-16.1	rim	0.10	121	7	0.06	334.3	3.7	0.05322	0.00060	0.3779	3.12	0.05322	1.12	0.359
A1553-19.1	rim	0.01	292	11	0.04	334.3	3.3	0.05322	0.00054	0.3860	2.09	0.05322	1.01	0.486
A1553-10.1	rim	0.00	72	44	0.63	336.7	4.8	0.05362	0.00078	0.4063	3.62	0.05362	1.25	0.345
A1553-18.3	rim	0.00	408	14	0.04	339.4	3.0	0.05407	0.00050	0.3912	1.80	0.05407	0.91	0.508
A1553-1.3	rim	0.09	154	7	0.05	339.5	3.5	0.05407	0.00057	0.3912	2.68	0.05407	1.04	0.390
A1553-21.2	rim	0.15	76	14	0.19	339.9	4.5	0.05414	0.00073	0.4275	4.34	0.05414	1.30	0.299
A1553-4.1	rim	0.00	311	170	0.56	341.4	3.7	0.05439	0.00061	0.4115	1.94	0.05439	1.01	0.522
A1553-18.1	rim	2.49	86	8	0.09	344.0	4.4	0.05481	0.00073	0.3552	7.14	0.05481	1.24	0.174
A1553-7.2	rim	0.08	118	21	0.19	345.0	5.0	0.05498	0.00082	0.3906	3.11	0.05498	1.45	0.465
A1553-12.1	rim	0.01	241	9	0.04	345.7	3.5	0.05510	0.00057	0.4116	2.18	0.05510	1.04	0.476
A1553-20.1	rim	0.06	305	10	0.03	346.2	3.2	0.05517	0.00053	0.3995	2.05	0.05517	0.96	0.468
A1553-13.1	rim	2.54	92	20	0.22	347.5	4.5	0.05539	0.00074	0.3841	8.21	0.05539	1.19	0.145
A1553-8.1	rim	0.00	813	18	0.02	348.9	2.9	0.05562	0.00048	0.4107	1.33	0.05562	0.86	0.647
A1553-6.1	core	0.14	193	86	0.46	351.7	6.6	0.05608	0.00108	0.4144	2.95	0.05608	1.78	0.602
A1553-9.2	core	0.39	237	103	0.45	395.7	4.1	0.06331	0.00067	0.4490	2.30	0.06331	0.97	0.424
A1553-20.2	core	0.00	231	141	0.63	412.0	4.4	0.06600	0.00073	0.5305	2.50	0.06600	0.99	0.395
A1553-18.2	core	0.03	202	99	0.51	422.0	4.5	0.06766	0.00074	0.5337	3.03	0.06766	1.00	0.331
A1553-22.1	core	0.36	232	119	0.53	430.5	4.6	0.06906	0.00077	0.5517	2.20	0.06906	1.01	0.462
A1553-17.1	core	0.00	209	116	0.57	435.5	5.7	0.06989	0.00094	0.5728	2.19	0.06989	1.22	0.558
A1553-8.2	core	0.14	109	33	0.31	440.0	8.2	0.07063	0.00137	0.5527	3.14	0.07063	1.84	0.584
A1553-14.1	core	0.00	296	166	0.58	447.9	5.0	0.07194	0.00082	0.5647	1.83	0.07194	1.04	0.568
A1553-1.2	core fractured	0.01	146	36	0.25	450.2	5.0	0.07234	0.00084	0.5732	2.29	0.07234	1.11	0.486
A1553-3.1	core	0.07	351	200	0.59	459.3	4.5	0.07385	0.00074	0.5924	1.61	0.07385	0.91	0.568
A1553-2.1	core	0.00	39	15	0.39	472.6	7.0	0.07607	0.00118	0.6432	4.34	0.07607	1.44	0.332
A1553-13.2	core	0.00	301	142	0.49	480.3	5.4	0.07735	0.00091	0.6090	1.80	0.07735	1.09	0.603
A1553-19.2	core	0.00	246	91	0.38	484.3	4.8	0.07802	0.00080	0.6195	1.90	0.07802	0.97	0.510
A1553-5.1	core	0.00	142	66	0.48	486.7	5.3	0.07842	0.00088	0.6320	2.28	0.07842	1.03	0.453
A1553-21.1	core	0.00	179	80	0.46	498.2	5.5	0.08035	0.00092	0.6447	2.18	0.08035	1.06	0.488
Mafic granulite (A1554)														
A1554-11.1	sector	0.08	339	24	0.07	320.4	3.0	0.05097	0.00048	0.3725	2.00	0.05097	0.94	0.469
A1554-5.1		0.01	1258	69	0.06	323.7	2.7	0.05150	0.00045	0.3745	1.27	0.05150	0.86	0.675
A1554-12.1		0.07	606	43	0.07	329.3	2.9	0.05241	0.00047	0.3904	1.61	0.05241	0.89	0.552
A1554-4.1	rim light	0.11	163	16	0.10	331.8	3.4	0.05281	0.00055	0.3857	2.52	0.05281	1.03	0.408
A1554-6.1	rim light	0.06	211	5	0.02	332.7	3.2	0.05296	0.00052	0.3880	2.30	0.05296	0.99	0.429
A1554-9.1		0.10	354	31	0.09	332.8	3.4	0.05298	0.00056	0.3981	1.95	0.05298	1.04	0.535
A1554-7.1		0.12	360	27	0.08	333.0	3.0	0.05301	0.00049	0.3988	2.29	0.05301	0.92	0.400
A1554-10.1	rim light	0.14	80	11	0.14	335.3	4.2	0.05339	0.00068	0.3794	3.75	0.05339	1.24	0.331
A1554-1.1		0.04	589	47	0.08	336.2	3.3	0.05354	0.00054	0.3907	1.59	0.05354	1.00	0.627
A1554-12.2		0.00	482	62	0.13	336.4	3.2	0.05357	0.00052	0.3907	1.76	0.05357	0.95	0.539
A1554-2.1		0.01	854	57	0.07	337.0	2.9	0.05367	0.00047	0.3848	1.33	0.05367	0.87	0.651
A1554-13.1		0.04	254	16	0.07	337.5	3.2	0.05374	0.00053	0.4121	2.20	0.05374	0.98	0.443
A1554-8.1		0.02	826	49	0.06	339.8	2.9	0.05413	0.00047	0.3977	1.35	0.05413	0.86	0.636
A1554-13.2		0.05	764	49	0.07	340.6	3.3	0.05426	0.00054	0.3923	1.54	0.05426	0.98	0.639
A1554-14.1		0.00	747	56	0.08	344.6	3.3	0.05490	0.00054	0.3997	1.56	0.05490	0.97	0.618
A1554-3.2		0.00	445	36	0.08	346.2	4.1	0.05517	0.00067	0.4076	1.87	0.05517	1.20	0.643
A1554-13.3	inherited core	0.26	82	28	0.35	377.7	6.2	0.06034	0.00103	0.4384	4.12	0.06034	1.60	0.387

Pb_c % = percent of common Pb

Table 3. LA-ICPMS analyses of zircons.

	A1554- 2core	A1554- 7core	A1554- 8core	A1554- 1core	A1554- 12core	A1554- 12a	A1554- 14core	A1554- 6rim	A1554- 3rim	A1554- 10rim	A1553- 1core	A1553- 4core	A1553- 3core	A1553- 6core	A1553- 21core	A1553- 20core	A1553- 19core	A1553- 1rim	A1553- 11rim	A1553- 21rim	A1553- 13rim	A1553- 15rim	A1553- 16rim
P	89	85	107	106	94	178	130	65	66	70	84	190	361	286	264	255	208	50	90	49	43	119	42
Ca	bdl	bdl	bdl	bdl	bdl	bdl	bdl	bdl	bdl	bdl	bdl	bdl	bdl	bdl	bdl	bdl	0.01	bdl	0.00	bdl	bdl	bdl	bdl
Ti	7.4	6.1	7.8	9.0	6.2	6.5	7.7	5.6	11	10.0	5.4	8.6	16.9	8.2	8.1	9.7	30	7.1	14	10.0	6.4	14	6.3
Sr	0.20	0.16	0.23	0.17	0.14	0.20	0.21	0.08	0.13	0.22	0.16	0.50	1.25	0.48	0.42	0.59	0.59	0.08	0.06	0.16	0.08	0.07	0.09
Y	380	286	564	311	180	452	444	86	49	68	185	1543	3403	1291	1673	1857	835	48	32	29	45	68	49
Nb	0.76	0.60	0.72	0.86	0.77	0.81	0.96	0.22	0.16	0.17	0.50	0.87	1.6	1.7	2.8	1.0	1.9	0.49	0.25	0.12	0.26	0.24	0.24
La	0.003	bdl	0.004	0.004	0.031	0.004	0.005	0.026	bdl	0.20	0.024	0.018	0.21	0.037	0.007	0.053	0.23	0.002	0.032	bdl	bdl	0.014	bdl
Ce	3.8	2.9	4.6	4.3	3.4	6.5	4.9	3.5	2.8	5.6	6.5	11.8	14.4	9.8	7.2	9.4	5.7	1.5	8.0	4.8	1.4	8.2	3.2
Pr	0.01	0.01	0.05	0.01	0.02	0.03	0.02	0.06	0.03	0.12	0.02	0.09	0.27	0.05	0.10	0.17	0.08	0.004	0.05	0.04	bdl	0.07	bdl
Nd	0.25	0.20	0.98	0.24	0.22	0.52	0.47	0.74	0.49	1.15	0.28	1.93	4.6	1.03	2.00	3.02	0.96	0.09	0.69	0.48	0.08	1.01	0.31
Sm	0.66	0.60	2.31	0.64	0.38	1.3	1.1	1.1	0.92	1.04	0.60	4.0	12	2.6	4.7	6.7	2.1	0.15	0.89	0.84	0.22	1.65	0.45
Eu	0.42	0.34	1.1	0.37	0.20	0.68	0.58	0.62	0.44	0.46	0.25	1.1	2.7	0.66	0.76	1.7	0.32	0.11	0.36	0.36	0.14	0.46	0.24
Gd	4.3	3.5	10.6	4.0	2.1	7.0	6.2	4.3	3.1	2.3	3.3	22	74	19	30	38.0	13.3	0.8	2.5	2.1	1.2	4.7	1.7
Tb	1.87	1.49	3.82	1.71	0.91	2.73	2.49	1.21	0.85	0.58	1.21	8.74	28	7.91	12	14	5.4	0.34	0.57	0.58	0.43	1.09	0.54
Dy	26	21	47	23	13	35	33	11	6.6	5.8	15	118	334	109	154	171	73	3.95	4.55	3.84	4.50	8.99	5.39
Ho	12	8.8	18	9.6	5.4	14	14	3.0	1.7	2.2	5.7	50	122	43	61	63	29	1.4	1.1	1.0	1.4	2.3	1.6
Er	63	46	87	50	29	74	72	11	5.4	10	28	250	524	211	269	287	136	5.7	3.3	2.8	5.3	7.1	5.8
Tm	17	12	21	13	7.7	18	18	1.9	0.9	2.5	7.1	60	109	48	60	63	31	1.2	0.6	0.47	1.1	1.3	1.0
Yb	212	148	247	155	93	215	223	16	7.7	29	84	638	1043	499	590	635	317	13	4.4	4.1	10	10	10
Lu	44	30	48	31	19	41	44	2.4	1.2	5.8	16	110	161	85	94	103	54	2.1	0.59	0.84	1.8	1.4	1.5
Hf	11827	11509	10880	10662	11313	10143	10640	9745	10810	8545	10472	9526	7779	8321	7913	8127	8766	10566	8394	8610	9760	7550	8853
Ta	0.53	0.44	0.59	0.53	0.70	0.35	0.54	0.05	0.02	0.04	0.25	0.35	0.60	0.63	0.90	0.38	0.97	0.15	0.05	0.03	0.08	0.04	0.08
Pb	2.0	1.1	3.1	1.4	1.3	1.7	1.8	0.10	0.37	0.50	1.5	5.8	6.9	3.4	3.3	4.3	2.2	0.20	0.62	0.52	0.15	0.63	0.38
Th	66	37	107	46	45	58	62	3.5	11	15	41	196	194	108	86	127	57	5.5	21	15	4.5	19	11
U	926	435	931	557	590	468	669	192	25	64	190	345	331	234	196	207	343	93	55	80	135	29	103
Th/U	0.07	0.09	0.12	0.08	0.08	0.12	0.09	0.02	0.46	0.24	0.21	0.57	0.59	0.46	0.44	0.61	0.16	0.06	0.38	0.18	0.03	0.66	0.11
(Lu/Gd) _N	82.7	69.6	36.7	62.4	71.1	47.8	58.2	4.6	3.1	20.7	39.9	39.5	17.6	36.4	25.6	21.9	32.6	20.0	1.9	3.2	12.2	2.4	7.0
(Eu/Eu*) _N	0.58	0.56	0.59	0.54	0.53	0.55	0.53	0.75	0.72	0.88	0.43	0.28	0.21	0.21	0.15	0.26	0.14	0.77	0.67	0.79	0.67	0.48	0.73

bdl = below detection limit

Eu* = (Gd+Sm)/2

The subscript "N" indicates values normalised to chondrite